

# Internship Report

## MeerKAT S1 Band Galactic Center Mosaic

Kamalpreet Kaur

Supervisor: Dr. Isabella Rammala  
Max Planck Institute for Radio Astronomy

# Contents

<b>1</b>	<b>Introduction</b>	<b>4</b>
1.1	Galactic Center . . . . .	4
1.2	Pulsars and their search in continuum . . . . .	5
1.3	Radio Interferometer Measurement Equation . . . . .	6
<b>2</b>	<b>Calibration Techniques</b>	<b>7</b>
2.1	First Generation Calibration . . . . .	7
2.2	Imaging . . . . .	8
2.3	Second Generation calibration . . . . .	9
<b>3</b>	<b>Analysis and Results</b>	<b>10</b>
3.1	Examining the data . . . . .	10
3.2	Manual Calibration of GC01-04 and comparison with OXKAT gaintables	13
3.2.1	Delay Calibration . . . . .	13
3.2.2	Bandpass Calibration . . . . .	13
3.2.3	Gain Calibration . . . . .	16
3.2.4	Scaling the amplitude gains . . . . .	16
3.3	Imaging: GC01-GC04 . . . . .	19

---

3.4	Primary Beam Correction . . . . .	22
3.5	Mosaic: GC01-04 . . . . .	23
3.6	Calibration of GC05-08 via MMGPS pipeline and its comparison with OXKAT gaintables . . . . .	24
3.6.1	Delay calibration . . . . .	24
3.6.2	Bandpass Calibration . . . . .	24
3.6.3	Gain Calibration . . . . .	25
3.6.4	Scaling the amplitude gains . . . . .	25
3.7	Imaging: GC05-GC08 . . . . .	30
3.8	Mosaic: Full extent of Galactic Center at S1 . . . . .	33
<b>4</b>	<b>Summary</b>	<b>34</b>
<b>5</b>	<b>Future Prospects</b>	<b>35</b>

# 1 Introduction

## 1.1 Galactic Center

Galactic Center (GC) is the central region of our Milky Way galaxy. It is a highly turbulent environment with filamentary magnetic fields, extremely dense gas, and numerous stars concentrated in clusters [5] as shown in Fig. 1. The GC is home to numerous supernova remnants (SNRs) since it contains massive stars that have short lifetimes, which would be leaving behind either neutron stars or stellar mass black holes depending on their masses.

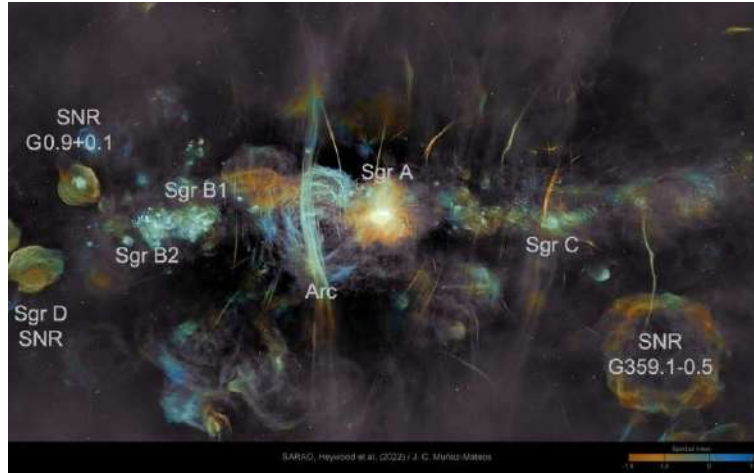


Figure 1: Galactic Center in radio wavelengths via MeerKAT colour coded by the spectral index. It comprises of the supernova remnants, HII regions, radio bright dynamic center believed to host the supermassive black hole Sgr A\* and non thermal radio filaments. The spectral index study helps to search pulsars in the continuum. Credits: [5]

It is beneficial to study GC in radio waves because radio wavelengths are unaffected due to the extinction effect of the foreground dust.

## 1.2 Pulsars and their search in continuum

A neutron star or a black hole remains at the heart of the SNR after a star dies during the course of stellar evolution with a rapid core collapse and destructive supernova explosion. Now, if the final object is a neutron star and its rotational axis is not aligned with its magnetic axis, the neutron star will release high-energy coherent synchrotron radiation beams from its magnetic poles. The neutron star is known as a pulsar when these beams are pointed towards the Earth and a pulsed emission is found as the neutron star sweeps through our line of sight [6].

We look for them in the GC because they can serve as probes for research into black holes and gravity tests. Additionally, they can be utilized to explore and learn more about the composition and structure of the ISM and the galactic magnetic fields.

We anticipate discovering a lot of pulsars in the GC due to the presence of a significant population of neutron stars there. In order to derive explanations and models of the observed effects in the GC region, it will be important to determine if there is a population of GC pulsars or not.

Due to survey limitations, it is possible that prior searches for GC pulsars were unsuccessful for a number of different reasons. Additionally, there may be significant difficulty in recognizing periodicity in time series data due to hyper-scattering along the line of sight between the observer and the pulsar [6]. This is as a result of the high projected electron content for the GC. As a result, scattering may make it impossible to conduct any periodicity searches at lower radio frequencies, while searches at higher frequencies are often hampered by the radio pulsar emission's frequently steep negative spectral index [9]. Additionally, pulse spreading across distinct filterbank frequency channels can reduce the capacity to identify pulses. Also, single-dish telescopes, which at high frequencies have smaller telescope beams and cover small areas, are typically used in pulsar search surveys and cover small regions of the sky.

We can look for them in the image domain, where they can be recognized as unresolved point sources due to the neutron star's physical size, to get over the difficulties associated with searching for them in areas with significant ISM. Regardless of the dispersion, a pulsar will be visible in the image domain. A candidate with pulsar-like qualities can be distinguished from other compact sources with spectral characteristics comparable to a pulsar using the morphological composition of its environment and its spectral index [9]. A wider portion of the sky can be viewed by using interferometry in the image domain and a synthesized beam that is larger than the primary beam of a single dish telescope.

### 1.3 Radio Interferometer Measurement Equation

The Radio Interferometer Measurement Equation (RIME) provides a rigorous mathematical basis for the development of novel calibration methods and techniques [13].

RIME for a twin interferometer as shown in Fig. 2 is described as:

$$V_{pq} = J_p B J_q^H \quad (1)$$

where  $V_{pq}$  represent the visibility matrix,  $B$  is the brightness matrix which tells us about the true visibility and the terms  $J_p$  and  $J_q$  represent the Jones matrices which accounts for the various propagation effects that a signal undergoes from source to the antenna and then from antenna to the correlator.

There is a chain of Jones matrices which comprises of various effects such as delay errors, atmospheric errors which are caused in the ionosphere and troposphere because of fluctuation in the electron densities and various instrumental errors.

Many calibration softwares included Common Astronomy Software Applications (CASA) works on the calibration principles of RIME [13].

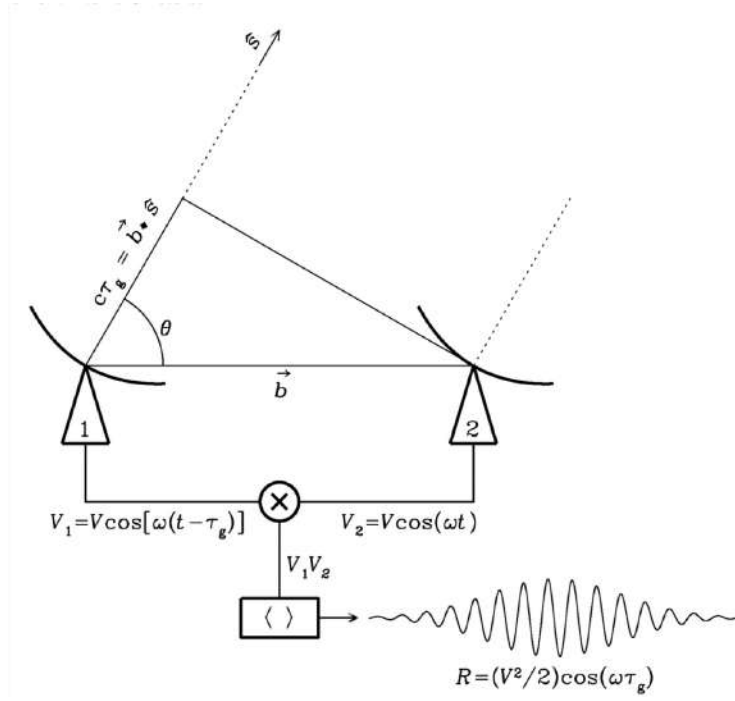


Figure 2: A basic two element interferometer where the antennas are collecting the signals from a source in voltages  $V_1$  and  $V_2$ . The voltages are then transferred to a correlator where they are multiplied and averaged over time. Credits: [2]

## 2 Calibration Techniques

### 2.1 First Generation Calibration

First Generation Calibration (1GC), also called as reference calibration, is the starting step where we correct for the large scale errors in the observed visibilities [10]. To do so, we assume a model spectrum of our flux calibrator and then derive solutions between observed visibilities and model visibilities. Then these solutions are applied to all our calibrators as well as target fields. 1GC comprises of delay, bandpass and

gain calibration. They will be explained in detail in section 3.2.

The flux calibrator or the primary calibrator is chosen to be a well modelled point source [7]. It is also used as delay, bandpass and gain calibrator. The observation for the flux calibrator is usually made at the beginning and the end of the observation because its flux remains unchanged over time during the course of the observation.

The phase calibrator or the secondary calibrator is usually chosen to be near the target fields so that it can mimic the environment of the target fields [9]. As its phases are well modelled, thus, it helps us to track the phase errors because of the movement of the antennas during the scan. Thus, we take observation of our phase calibrator at the beginning as well as at the end of our target field and before moving to the other one.

## 2.2 Imaging

The process of transferring the Fourier measurements from the visibility domain to the image domain is known as imaging [7]. The radio interferometer sees the Fourier transform of the sky brightness distribution which has to be transformed back into the image domain to recover this brightness distribution. The image that we receive after this is known as the dirty image which is the convolution of the true image with the point spread function of the telescope [10]. This dirty image thus has the response of side lobes in it. To clean this dirty image and to reduce the systematical and statistical noise in the image is what is called as deconvolution. This is performed by *wsclean* which uses the w-stacking algorithm to do the inverse Fourier Transform and deconvolution to produce true images [8].

To get a good image, one needs to be careful with setting up the imaging parameters. The size of the image is decided by seeing the total coverage of the uv wavelength. The best cleaning is done with 4-5 pixels across the synthesized beam, which gives us the pixel size [7]. Weighting of the image also helps to improve the image fi-



delity. Natural weighting gives an equal weighting to each sampled visibility. This increases sensitivity and decreases angular resolution. Uniform weighting gives all gridded visibility cells with the same weighting, no matter how many times that uv cell was sampled [8]. This gives more weight to longer baselines and improves angular resolution but at the same time decreases sensitivity. Briggs weighting is a compromise between uniform and natural weighting, which is set using the robust parameter which can be any value between -1 to 1 generally [8].

## 2.3 Second Generation calibration

In the 1GC, the large scale errors in the observed visibilities are corrected using a model spectrum. Now, it is possible that the model spectrum would not be the best model with changing time and frequency of observation. Also, it is possible that the phase calibrator does not mimic the target's environment completely. Thus to correct for that, we do second generation calibration (2GC), also known as self calibration.

In self calibration, we assume a model by imaging the data itself, to correct for the additional phase errors in the images. This model is generated by creating a mask using the image where one includes most of the emission from the target without including much of the spurious sources [9]. One can do many rounds of self calibration, by the time, the dynamic range of the image keeps improving. Dynamic range is defined as the maximum value in Jy/beam divided by the rms value of the image [7]. For each round of self calibration, the solution interval should decrease, so that we can track the minute phase differences and correct for them [10].

### 3 Analysis and Results

#### 3.1 Examining the data

The data used in this internship is a part of the science demonstration project using the S1 band receiver of MeerKAT telescope with a frequency range of 1968-2843 MHz [12], central frequency at 2.4 GHz and a bandwidth of 851 MHz. There are 8 pointing in total, GC01-08. The data is averaged to 1024 channels and the calibrators used are the standard calibrators of MeerKAT, tracked by the observatory. The primary calibrator is J1939-6342 and the secondary calibrator is J1733-1304.

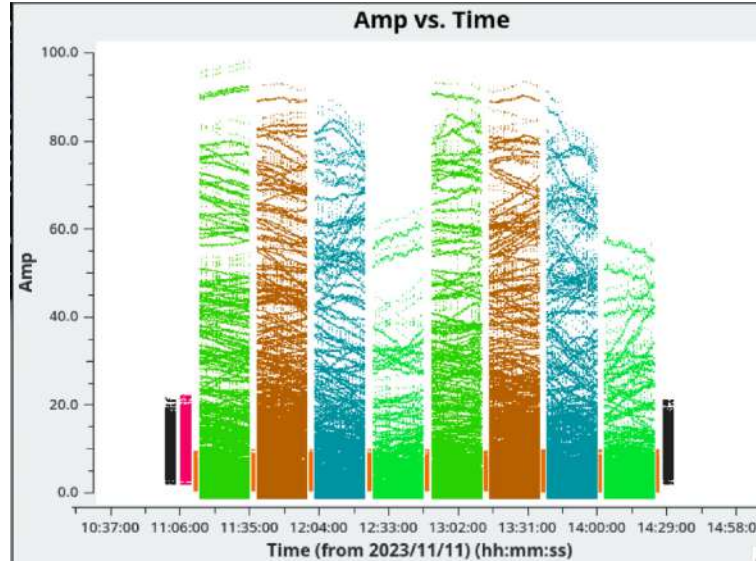


Figure 3: Overview of the observation, colour coded by the field. The primary calibrator (black) is observed in the beginning and the end of the observation. The targets are observed twice with 20 mins each, so 40 mins in total. The phase calibrator (pink) is observed after every target observation.

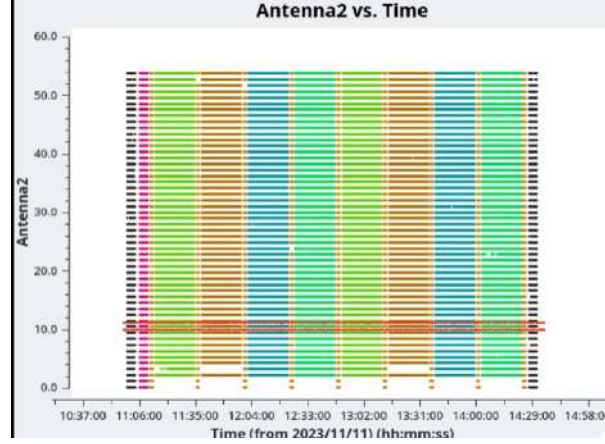


Figure 4: The datastream plot showing antennas vs time, colour coded by the field. The reference antenna chosen is m013 marked by red block in the figure because it has a consistent observation with time and also lies in the compact central core of the array. The location of m013 in the compact central core provides us with shorter baselines thus less atmospheric fluctuations with time.

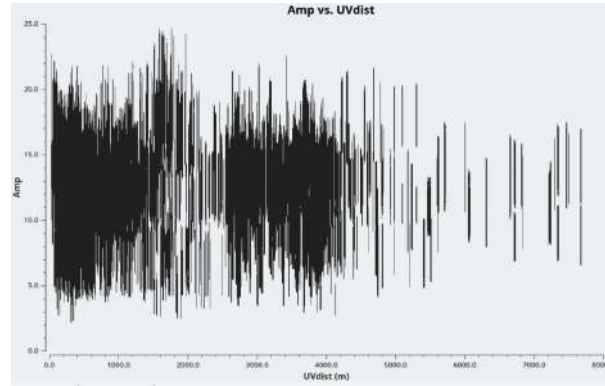


Figure 5: The amplitude vs uv distance of the primary calibrator. A relatively constant visibility amplitude as a function of baseline length means that the source is very nearly a point source. The Fourier transform of a point source, i.e. a delta function, is a constant function.

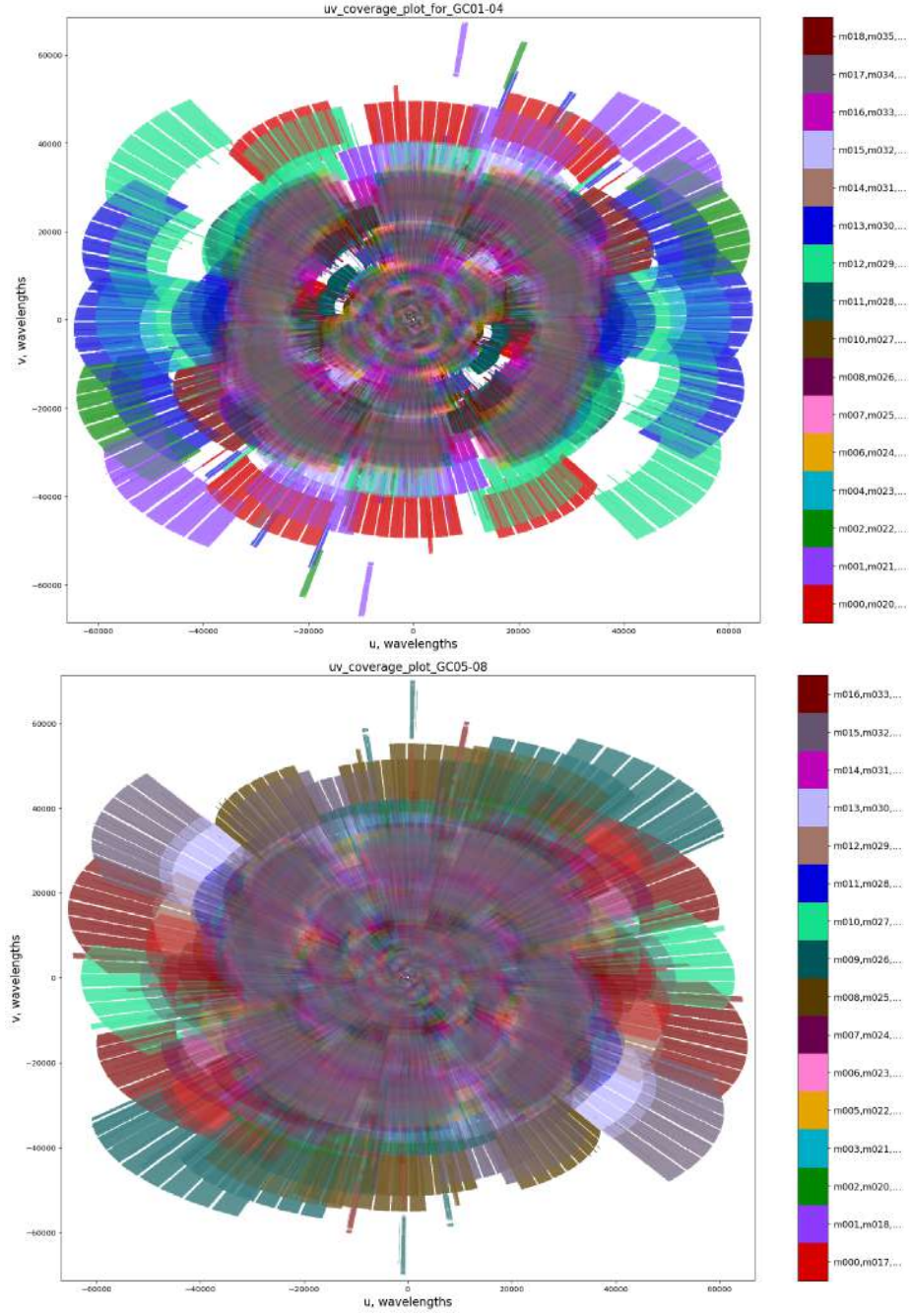


Figure 6: The image on the top is uv coverage of the pointings GC01-04 and the one on the bottom is the uv coverage of the pointings GC05-08. Both of them are colour coded by antenna. The uv coverage is more filled for GC05-08 because it had more number of antennas, 61, during the observation in comparison to GC01-04, which had 54 antennas at the time of the observation.

## 3.2 Manual Calibration of GC01-04 and comparison with OXKAT gaintables

### 3.2.1 Delay Calibration

We correct for the geometric delay of the signals at the antennas which causes a phase ramp versus frequency. We correct for relative delays of each antenna relative to the reference antenna. For this we chose the widest possible frequency channel range because they have lower sensitivity [7]. For manual calibration, the delays are within 0.15 ns and for gaintables via OXKAT, they are also approximately between 0.15 ns only. In manual calibration, it is two points because it was solved for solution interval as ‘inf’ and combine scan, which produces one solution per time per scan. In the pipeline, there are multiple points because it is possible that they are not using solution interval as ‘inf’ but some other integration factor. The delay calibration solutions from both of them are shown in Fig. 7.

### 3.2.2 Bandpass Calibration

The bandpass solutions account for gain variations with frequency which are caused because of different antenna bandpasses or transmission of signal strength [7]. So, when we use the task bandpass, it corrects for that. Hence, we should get a relatively flat function of amplitude and phase with frequency (channels). We are getting this for both (using pipeline and manual calibration), just that the channels are 100-1000 in pipeline and 200-800 in manual calibration. So, the bandpass task is working fine on the data as shown in Fig. 8.

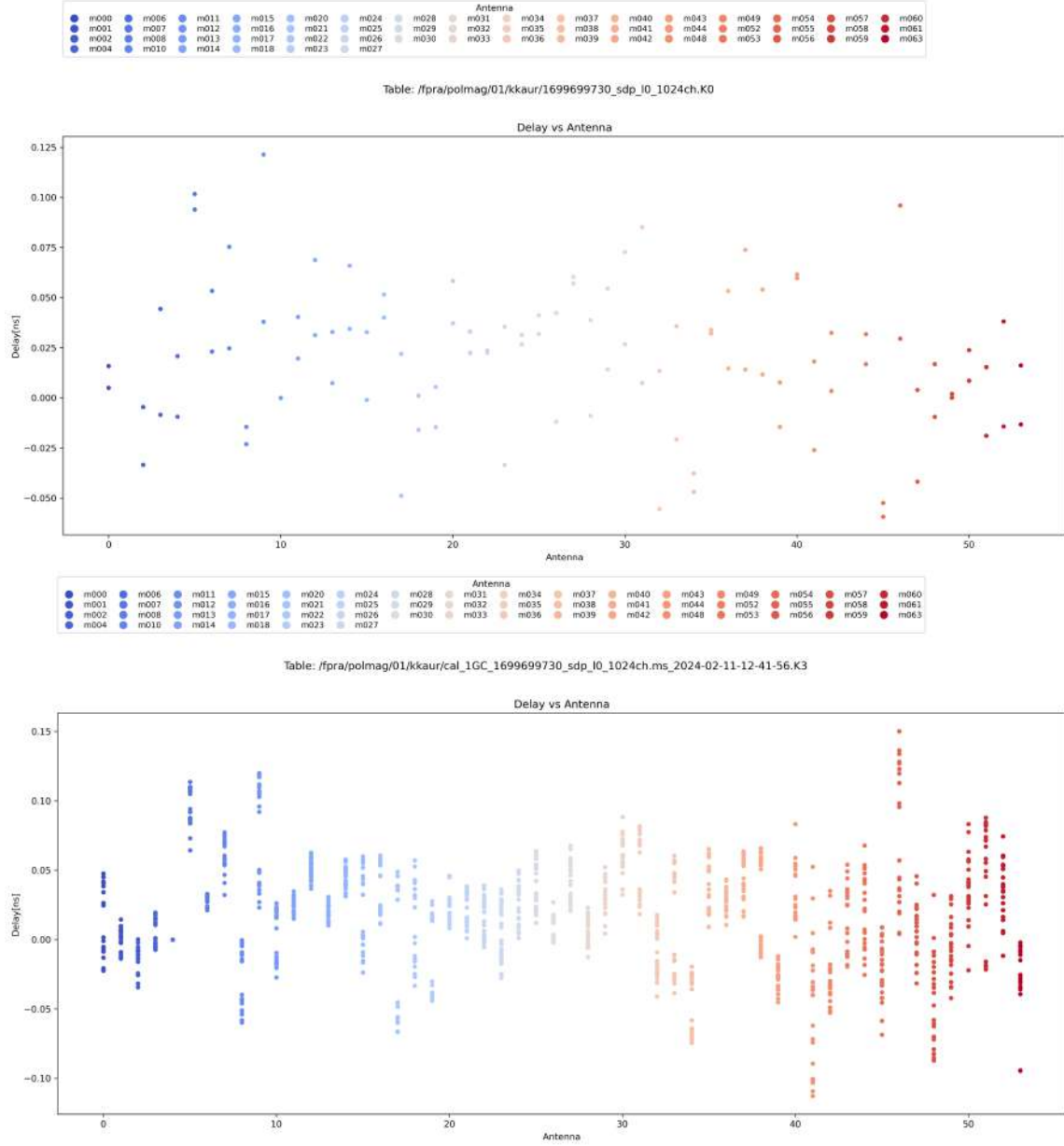


Figure 7: The image on the top is for delay calibration done manually while the one on the bottom is for delay calibration done via the OXKAT pipeline. The delay solutions are between 0.15 ns for both of them.



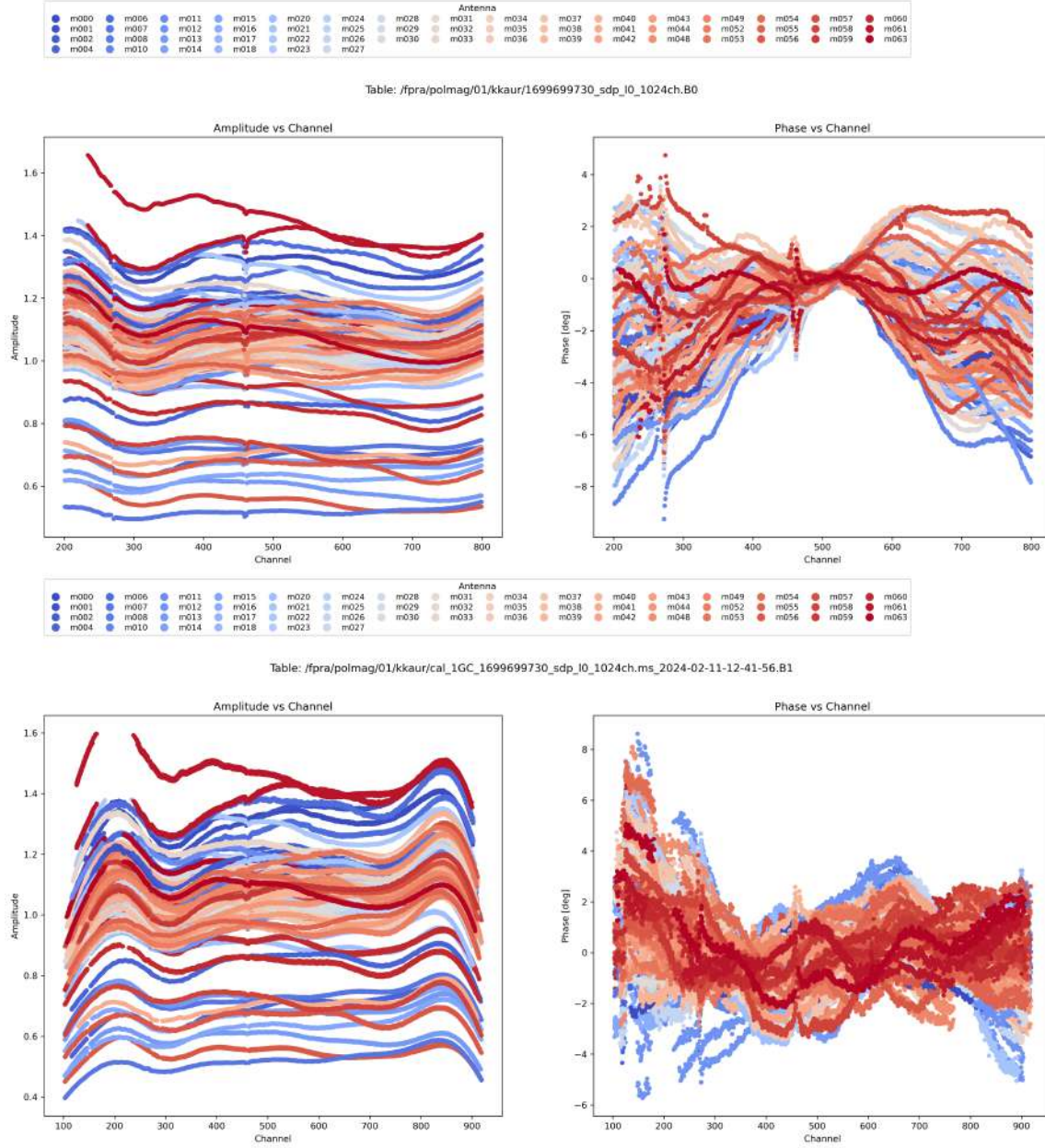


Figure 8: The image on the top is for bandpass calibration done manually while the one on the bottom is for bandpass calibration done via the OXKAT pipeline. Amplitude/Phase as a function of frequency. Amplitudes are relatively flat. Phase excursions are on the order of a few degrees.

### 3.2.3 Gain Calibration

Gain calibration corrects for the amplitude and phase variations from antenna to antenna as a function of time because of the electronic effects induced in signal transmission from antennas to correlators [7]. In the gain phase vs time graph, we see that there is smooth variation of gain phase with time. In manual calibration, it is around  $-150^\circ$  to  $150^\circ$ , meaning it requires high gain phase solutions and for the pipeline calibration it is between around  $-50^\circ$  to  $50^\circ$ , which is much better. Also using the task setJy, we set the amplitude of the flux calibrator to that of the model (value = 1.0). For the phase calibrator, we see that the gain amplitude has a larger value. This is because it is fainter and thus leading to higher solution values. This can be corrected using flux scaling task. The gain solutions via both methods are shown in Fig. 9.

### 3.2.4 Scaling the amplitude gains

We have a primary calibrator which is a standard bright source in the sky and then we have a phase calibrator close to our target which basically mimics the environment of our target. However, it will not be exactly the same and will vary with time, but this is an assumption we make for calibration purposes. Hence, using task fluxscale, we scale the flux density of the secondary calibrator (which is unknown) to our primary calibrator (which is known via a model). Hence, the gain solutions of amplitude are also scaled and thus both the sources should be approximately 1, which is happening in both the cases: in manual calibration as well as calibrating using the pipeline. They are shown in Fig. 10.



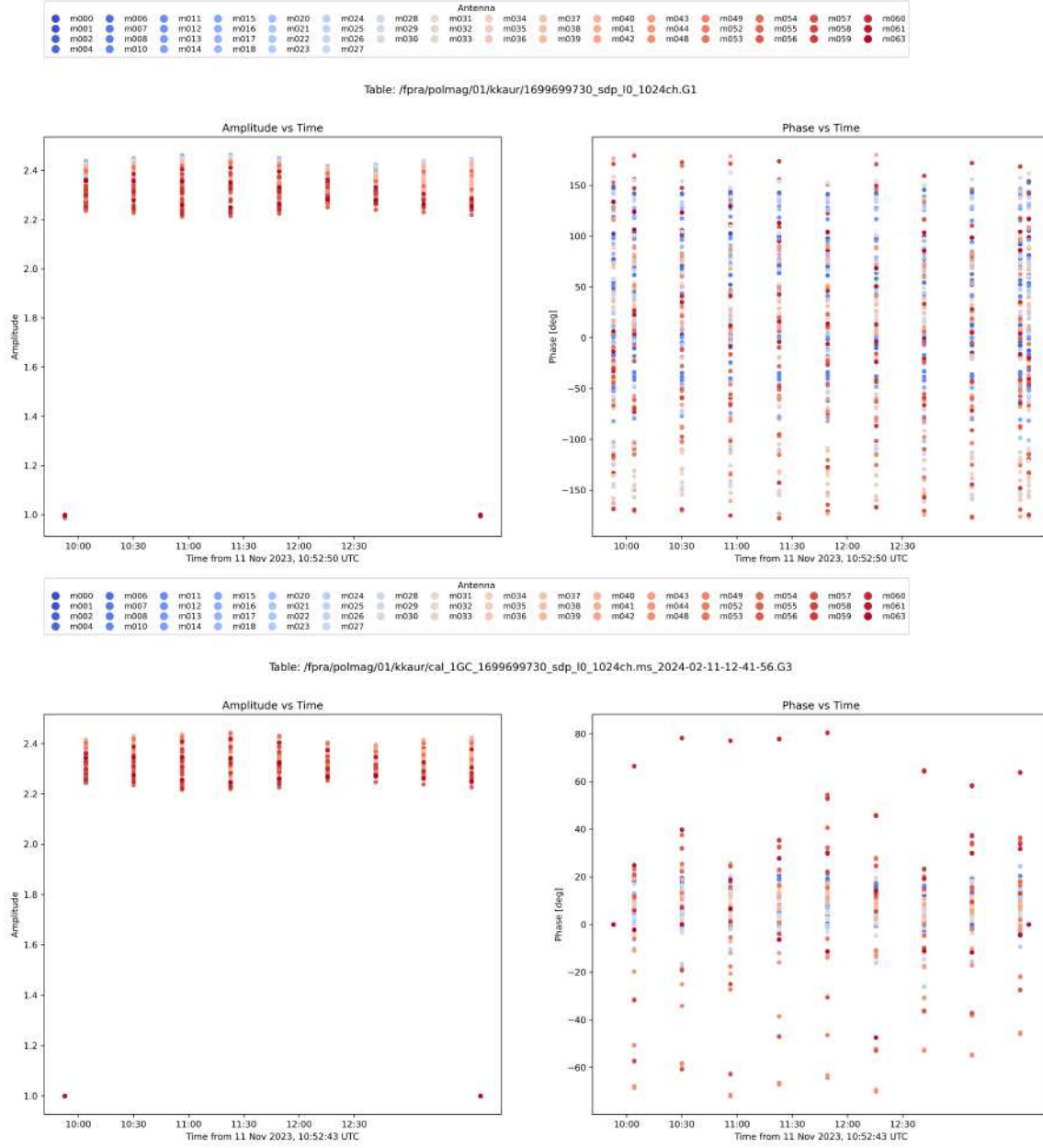


Figure 9: The image on the top is for gain calibration done manually while the one on the bottom is for gain calibration done via the OXKAT pipeline. Amplitude/Phase as a function of time. Smooth phase solutions for each antenna as a function of time. The lower gain solutions (approximately 1) are of the primary calibrator and those for the secondary calibrator are approximately 2.4 because it is dimmer.

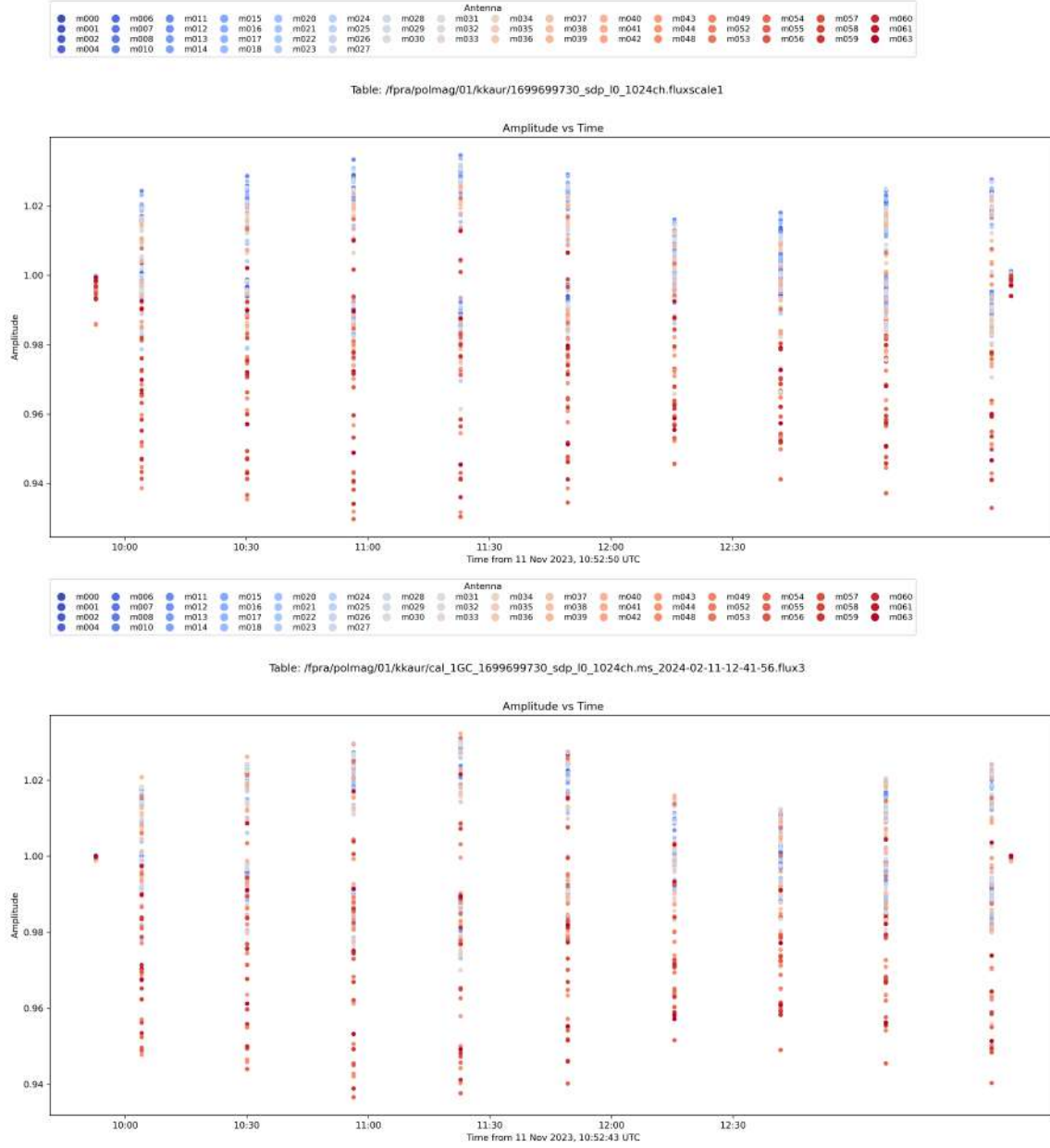


Figure 10: The image on the top is for scaled gain amplitudes done manually while the one on the bottom is for scaled gain amplitudes done via the OXKAT pipeline. The scaled amplitudes for the phase calibrator are approximately close to flux calibrator for both of them.

### 3.3 Imaging: GC01-GC04

We did a very shallow deconvolution run on the splitted target files with 30,000 iterations. After the first run, the images had phase errors, which were corrected with 3 rounds of self calibration followed by 5 rounds of deconvolution with 30,000 iterations in each run as shown in Fig. 11, 12 , 13 and 14. Before the beginning of each round, we created a mask using the input image via *make\_threshold.py* script provided by OXKAT, which was used as a model image to improve the image fidelity. We don't clean the images further because the GC is a very complex region and we cannot achieve a gaussian residual even after many rounds of deconvolution.

The maximum baseline was approximately 68000  $\lambda$ , which gave us the smallest angular resolution of 3". As the most effective cleaning happens with 4-5 pixels across the synthesized beam [7], thus, the pixel size taken was 0.6". The image was made to be of 7500 $\times$ 7500 pixels. We did multi scale cleaning with Briggs weighting of a robust parameter of 0.5. We also did multi frequency cleaning by splitting our target into 8 sub-bands and then averaged them together in a multi frequency synthesized image. All of this was done using the commands available in *wsclean* for the same.

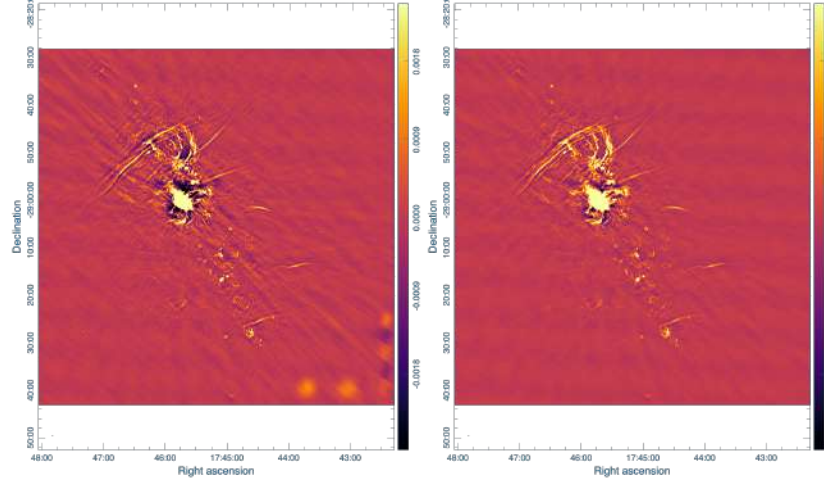


Figure 11: Pointing GC01. The image on the left is a shallow deconvolved image. The image on the right is the one obtained after 3 rounds of self calibration, followed by 5 rounds of deconvolution.

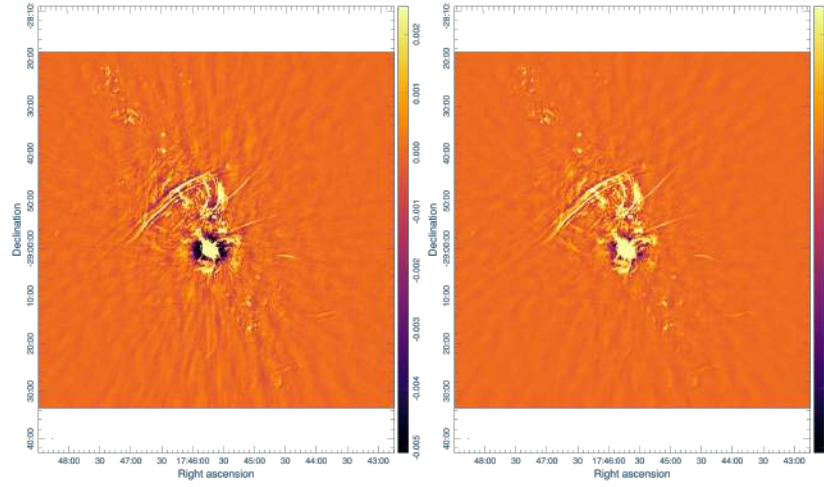


Figure 12: Pointing GC02. The image on the left is a shallow deconvolved image. The image on the right is the one obtained after 3 rounds of self calibration, followed by 5 rounds of deconvolution.

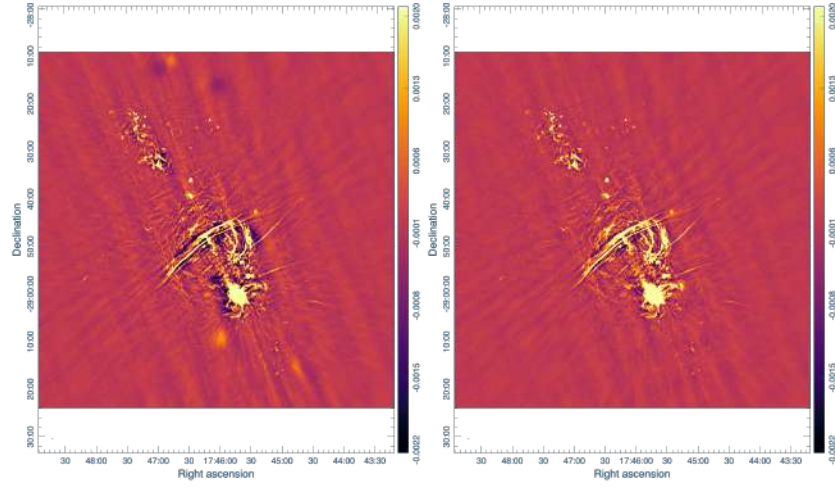


Figure 13: Pointing GC03. The image on the left is a shallow deconvolved image. The image on the right is the one obtained after 3 rounds of self calibration, followed by 5 rounds of deconvolution.

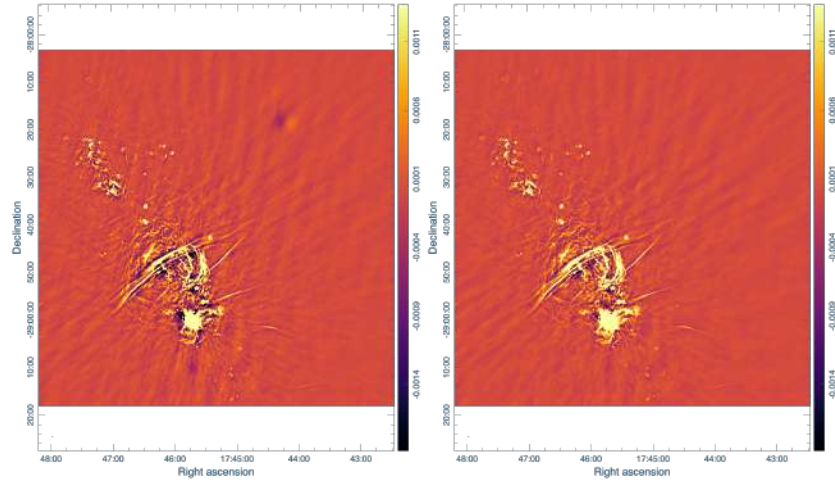


Figure 14: Pointing GC04. The image on the left is a shallow deconvolved image. The image on the right is the one obtained after 3 rounds of self calibration, followed by 5 rounds of deconvolution.

### 3.4 Primary Beam Correction

We constructed the primary beam response of our telescope at S1 band, the primary beam corrected image as shown in Fig. 15 which is the image averaged by the primary beam response of our telescope and weighted image (variance weighting) using the *katbeam* library from OXKAT.

The primary beam decreases (is sensitive) around the edges, so primary beam correction adjusts the observed image to account for this decrease in sensitivity at the edges of the telescope's point of view [7].

By using the weighted square of the primary beam, the contributions of each pointing to the final combined image is optimized as regions closer to the center of the primary beam contribute more significantly.

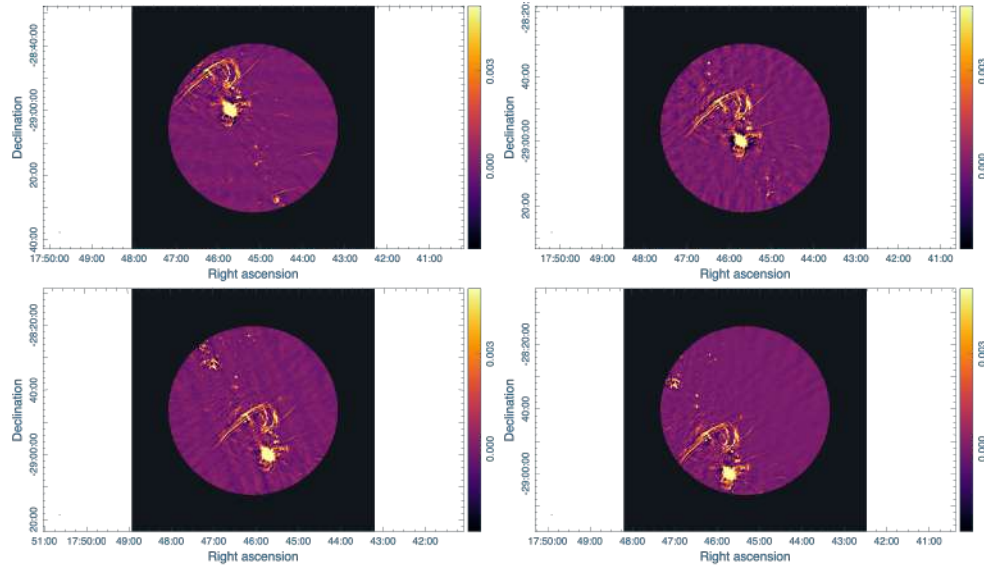


Figure 15: The primary beam corrected images of the Galactic Center pointings GC01 (top left), GC02 (top right), GC03 (bottom left) and GC04 (bottom right).

### 3.5 Mosaic: GC01-04

#### **very good explanation of all the steps in the montage tutorial**

Using the software tool *MONTAGE*, we assembled our primary beam corrected images into a mosaic. For that, we first created a metadata table for our input images. We processed the image metadata table to create a header file that described the footprint of the mosaic on the sky in FITS/WCS convention. This header will become the FITS header of the final mosaic. Then, we reprojected the input images to the specifications for the mosaic followed by creating a new metadata table that contains the updated header information in the reprojected files. Then, we finally added them in a mosaic as shown in Fig. 16.

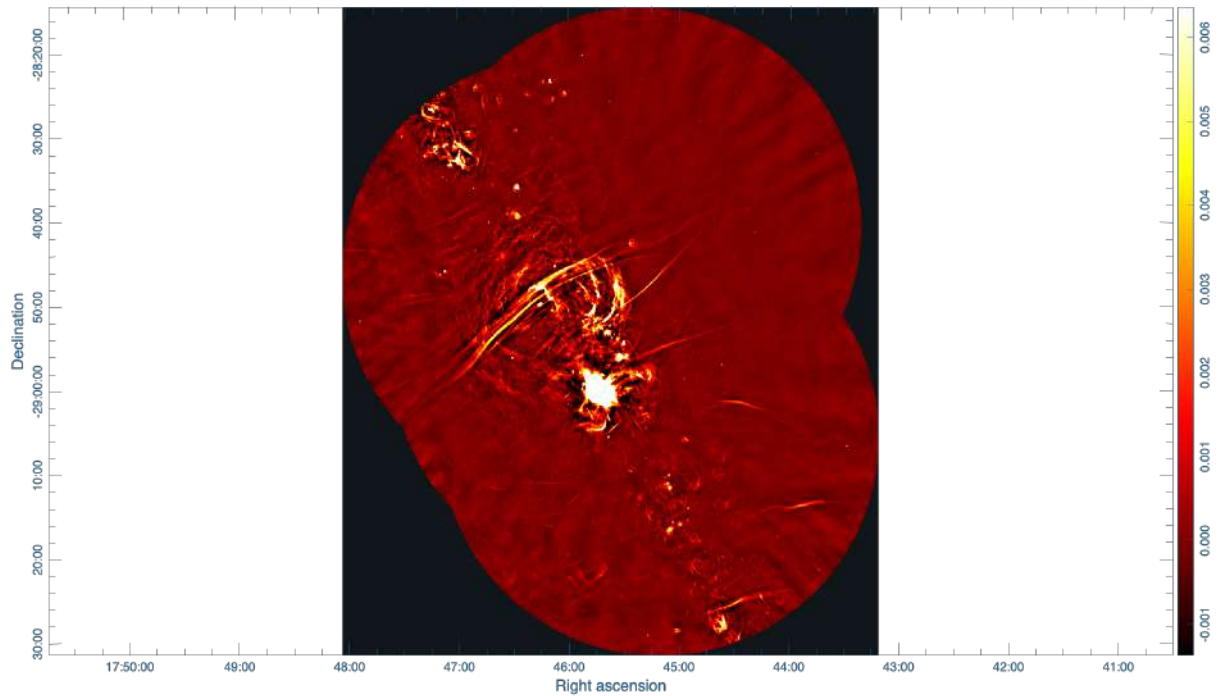


Figure 16: The extent of the Galactic Center pointings GC01-04 at S1 Band of MeerKAT. The images used are primary beam corrected with variance weighting applied to the mosaic.



### 3.6 Calibration of GC05-08 via MMGPS pipeline and its comparison with OXKAT gaintables

The MMGPS pipeline is the in-house radio imaging pipeline of the Max Planck Institute for Radio Astronomy (MPIfR). The pipeline works on the parameters mentioned in the configuration file and creates calibrated measurement set, does self calibration, produces high and low resolution images and mosaics. It works with 4k averaged channel data.

The pipeline does many rounds of flagging using the different flagging modes of the CASA: rflag, tfcrop and extend. It splits the data into 16 spectral windows, where each has around 227 channels in it. After calibration, it itself does rounds of flagging to flag the data with bad solutions. We compared the products of the 1GC from MMGPS with those of the OXKAT for pointings GC05-08 as shown in Fig. 17, 18, 19 and 20.

#### 3.6.1 Delay calibration

We correct for the geometric delay of the signals at the antennas which causes a phase ramp versus frequency. We correct for relative delays of each antenna relative to the reference antenna. The delays are within 0.15 ns for gaintables via OXKAT. For MMGPS, they are between 1-3 ns. The delay calibration solutions from both of them are shown in Fig. 17.

#### 3.6.2 Bandpass Calibration

The bandpass solutions account for gain variations with frequency which are caused because of different antenna bandpasses or transmission of signal strength [7]. So, when we use the task bandpass, it corrects for that. Hence, we should get a relatively



flat function of amplitude and phase with frequency (channels). We are getting this for both pipelines as shown in Fig. 18.

### 3.6.3 Gain Calibration

Gain calibration corrects for the amplitude and phase variations from antenna to antenna as a function of time because of the electronic effects induced in signal transmission from antennas to correlators [7]. In the gain phase vs time graph, we see that there is smooth variation of gain phase with time. For OXKAT, it is between approximately  $-50^\circ$  to  $50^\circ$  and for MMGPS,  $75^\circ$  to  $-150^\circ$ , meaning it requires high gain phase solutions. For the phase calibrator, we see that the gain amplitude has a larger value as compared to primary calibrator. This is because it is fainter and thus leading to higher solution values. This can be corrected using flux scaling task. The gain solutions via both methods are shown in Fig. 19.

### 3.6.4 Scaling the amplitude gains

We have a primary calibrator which is a standard bright source in the sky and then we have a phase calibrator close to our target which basically mimics the environment of our target. However, it will not be exactly the same and will vary with time, but this is an assumption we make for calibration purposes. Hence, using task fluxscale, we scale the flux density of the secondary calibrator (which is unknown) to our primary calibrator (which is known via a model). Hence, the gain solutions of amplitude are also scaled and thus both the sources should be approximately 1, which is happening in both the cases i.e. via OXKAT as well as MMGPS. They are shown in Fig. 20.

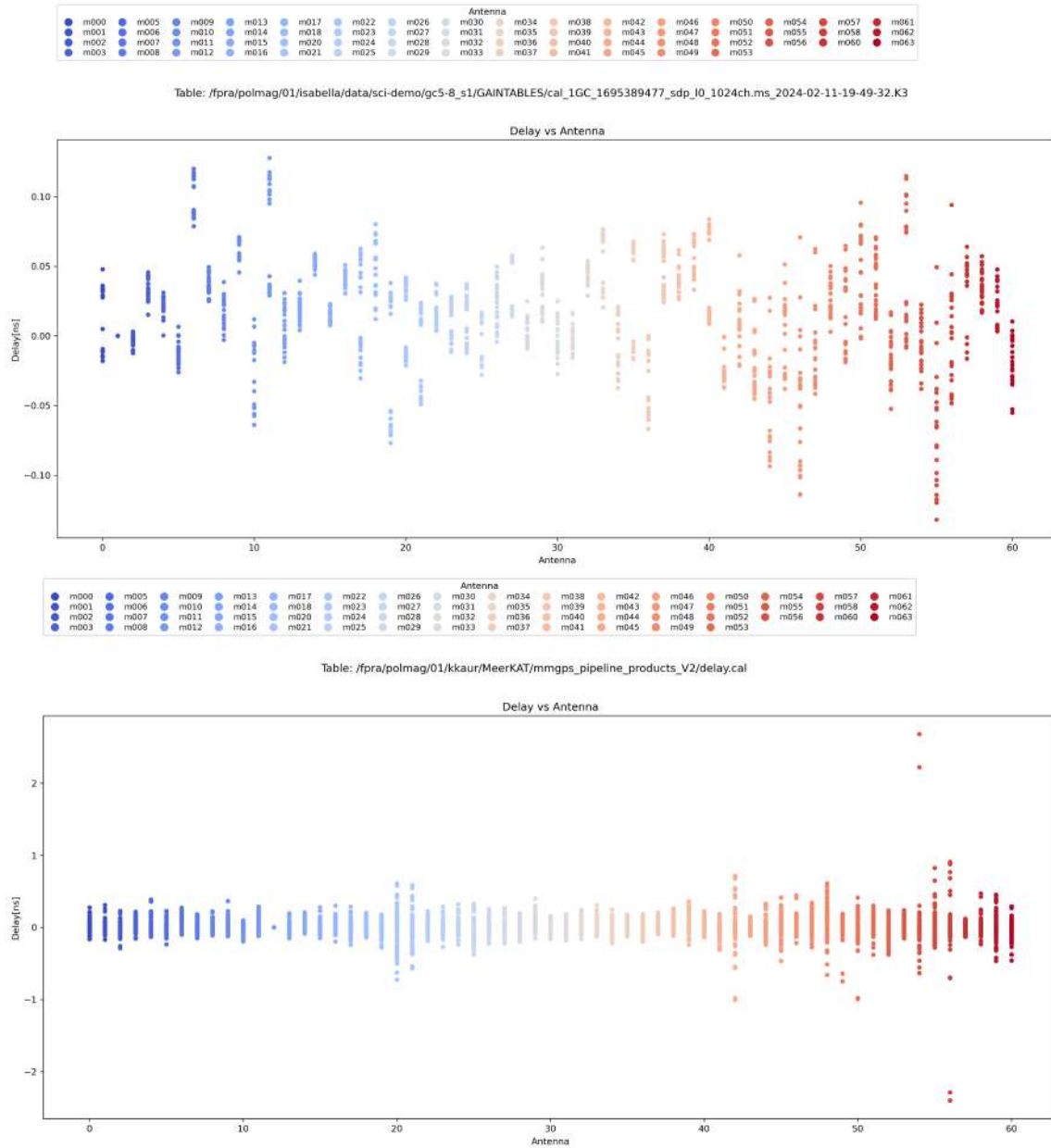


Figure 17: The image on the top is for delay calibration done via OXKAT pipeline and the one on the bottom is for delay calibration done via the MMGPS pipeline. The delay solutions are between 0.15 ns via OXKAT and 1 ns via MMGPS with exceptions of antennas 48 and 50, which go till 3 ns delay solutions.

**from next time, mention antenna names properly rather than numbers.**

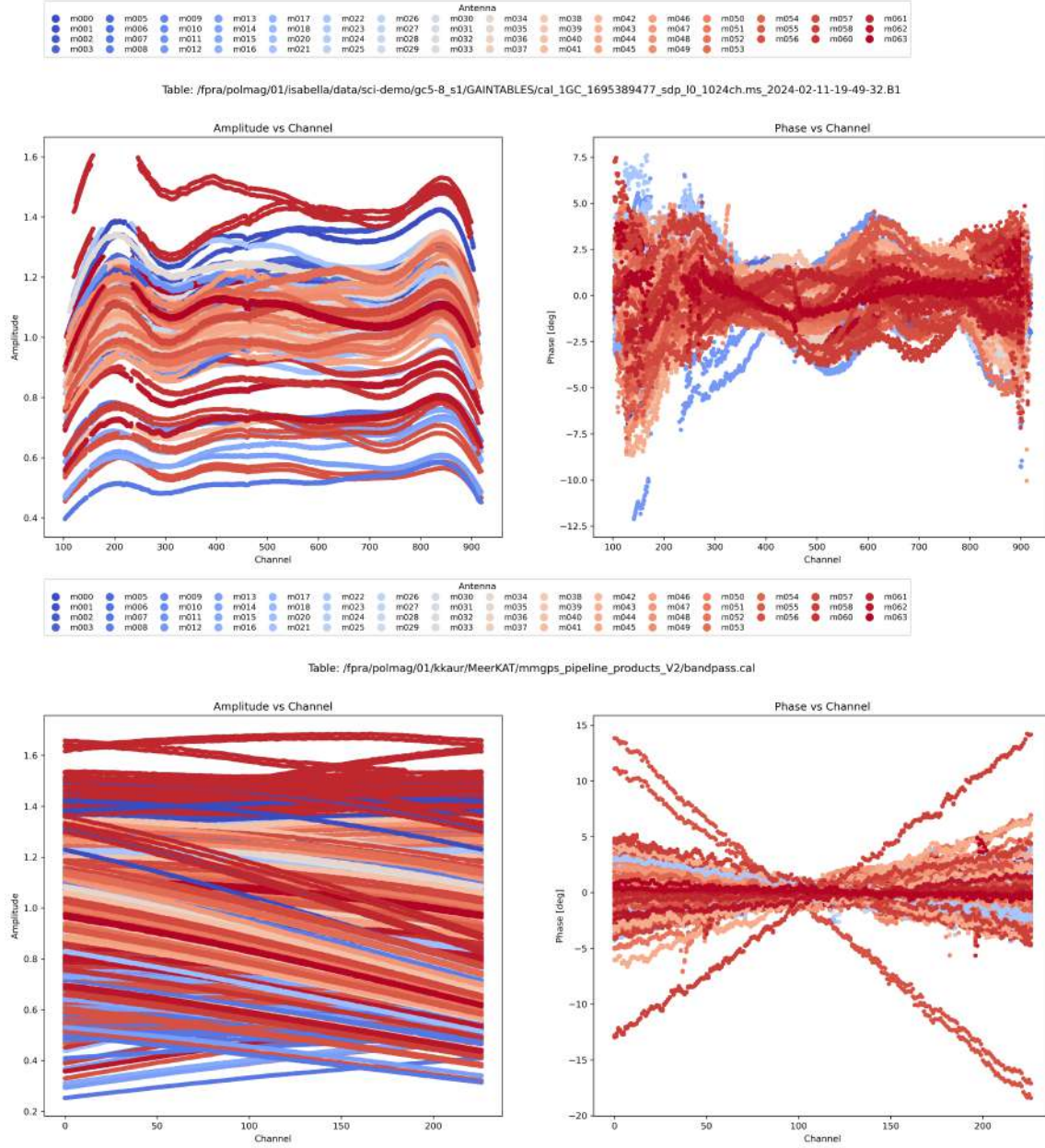


Figure 18: The image on the top is for bandpass calibration done via OXKAT pipeline and the one on the bottom is for bandpass calibration done via the MMGPS pipeline. Amplitude/Phase as a function of frequency. Amplitudes are relatively flat. Phase excursions are on the order of a few degrees. The channels for MMGPS are around 200 because it is the view of only first spectral window. For two antennas, the phase excursion is around  $30^\circ$ , which should be further taken care off by the MMGPS pipeline itself.

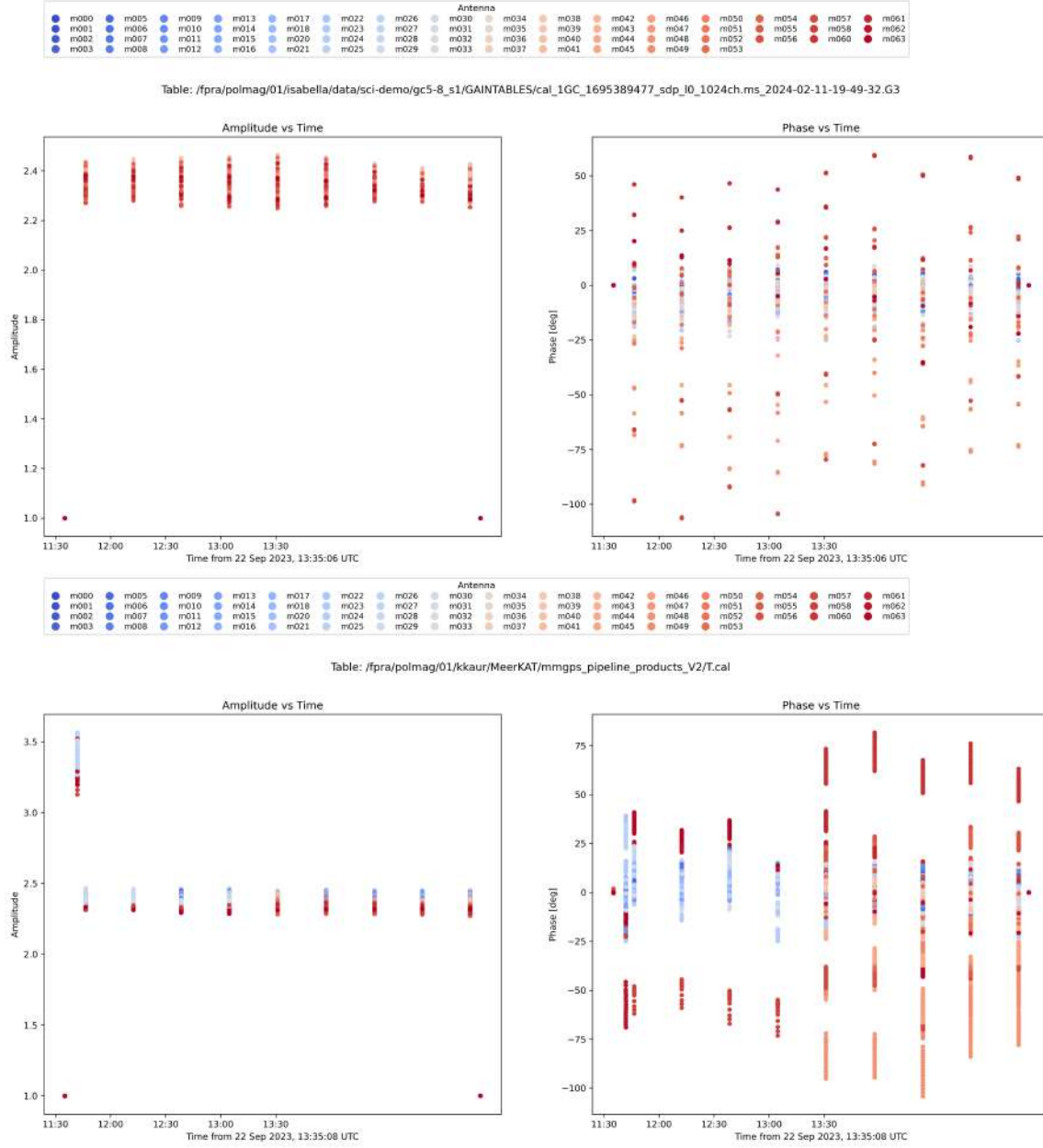


Figure 19: The image on the top is for gain calibration done via OXKAT pipeline and the one on the bottom is for gain calibration done via the MMGPS pipeline. Amplitude/Phase as a function of time. Smooth phase solutions for each antenna as a function of time. The lower gain solutions (approximately 1) are of the primary calibrator and those for the secondary calibrator are approximately 2.4 because it is dimmer.

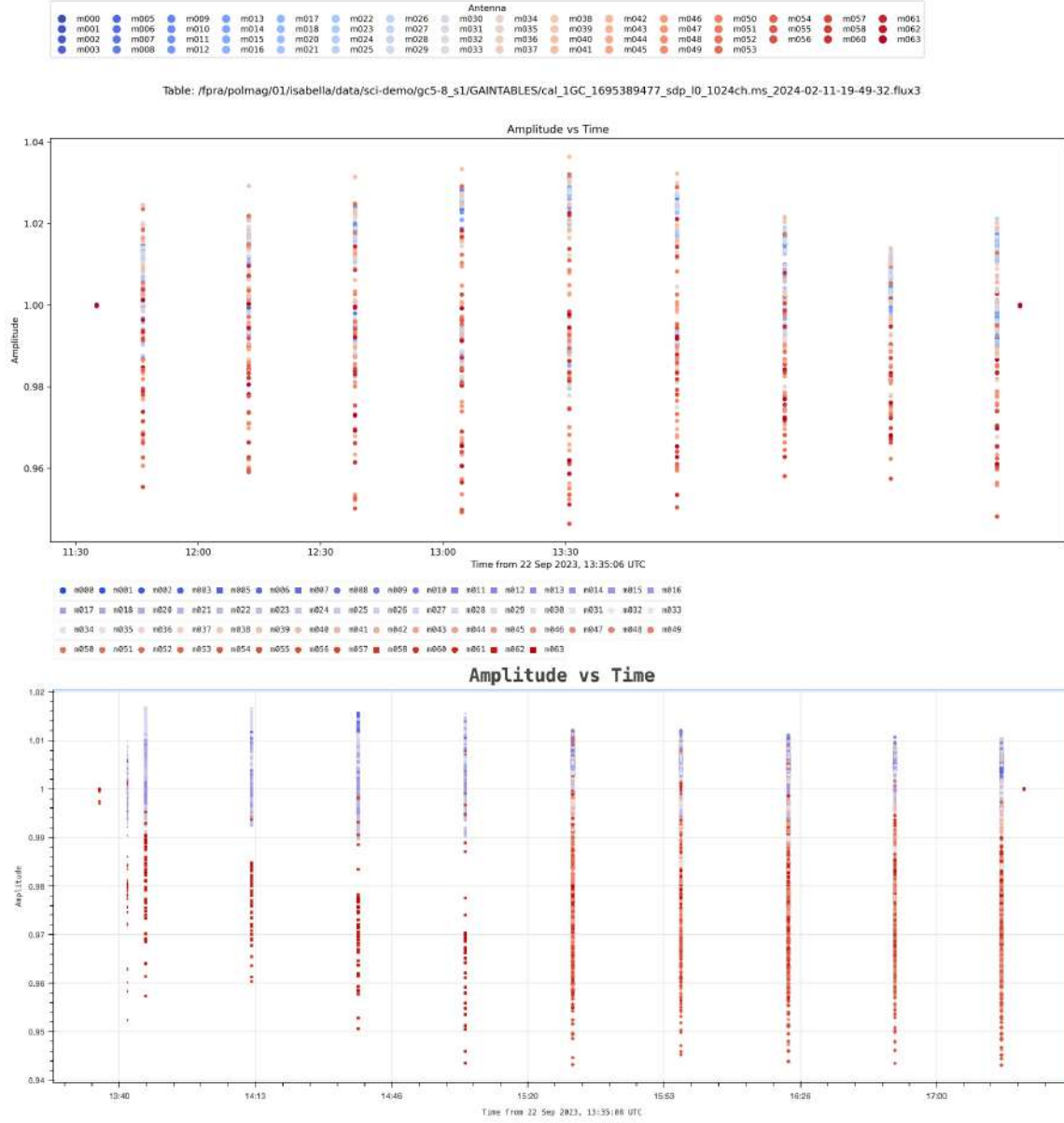


Figure 20: The image on the top is for scaled gain amplitudes done via OXKAT pipeline and the one on the bottom is for scaled gain amplitudes done via the MMGPS pipeline. The scaled amplitudes for the phase calibrator are approximately close to that of flux calibrator for both of them.

### 3.7 Imaging: GC05-GC08

We did a very shallow deconvolution run on the splitted target files with 30,000 iterations. After the first run, the images had phase errors, which were corrected with 3 rounds of self calibration followed by 3 rounds of deconvolution for GC05 and GC06, and 2 rounds of deconvolution for GC07 and GC08, with 30,000 iterations in each run as shown in Fig. 21, 22, 23 and 24. We aimed to do 5 rounds of deconvolution for all of them, but weren't able to reach our target because of the limited time duration for the internship.

Before the beginning of each round, we created a mask using the input image via *make\_threshold.py* script provided by OXKAT, which was used as a model image to improve the image fidelity. We don't clean the images further because the GC is a very complex region and we cannot achieve a gaussian residual even after many rounds of deconvolution.

The image was made to be of  $10,000 \times 10,000$  pixels with a pixel size of  $0.6''$ . We did multi scale cleaning with Briggs weighting of a robust parameter of 0.5. We also did multi frequency cleaning by splitting our target into 8 sub-bands and then averaged them together in a multi frequency synthesized image. All of this was done using the commands available in *wsclean* for the same.



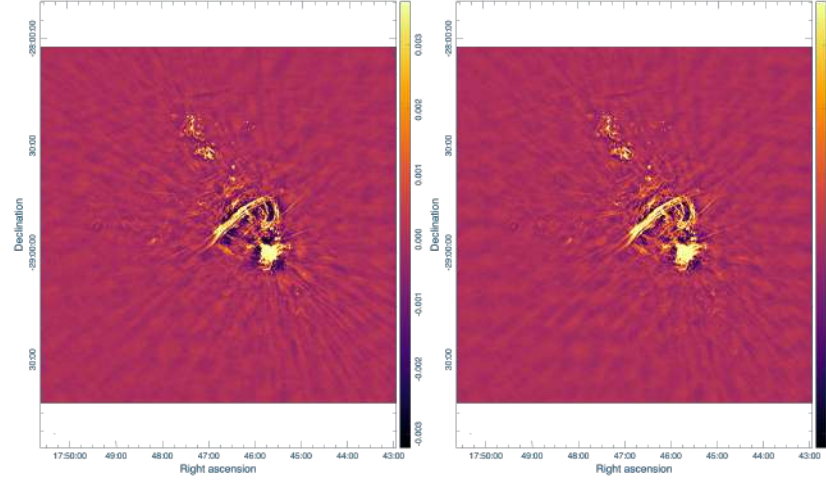


Figure 21: Pointing GC05. The image on the left is a shallow deconvolved image. The image on the right is the one obtained after 3 rounds of self calibration, followed by 3 rounds of deconvolution.

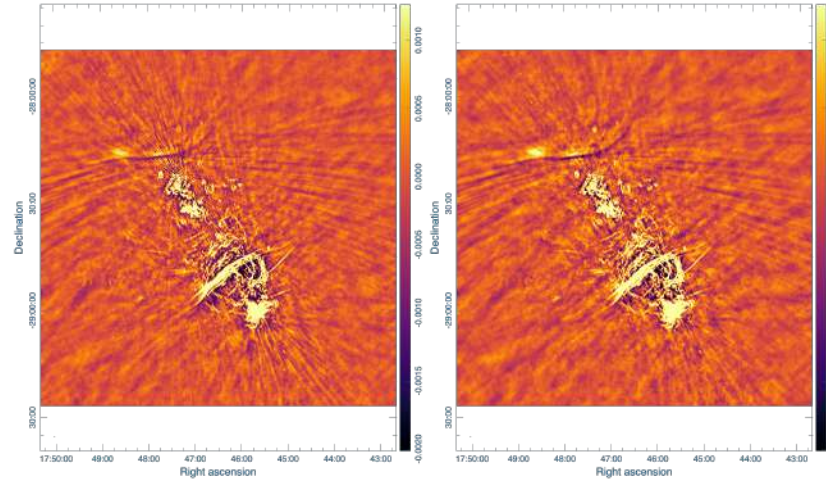


Figure 22: Pointing GC06. The image on the left is a shallow deconvolved image. The image on the right is the one obtained after 3 rounds of self calibration, followed by 3 rounds of deconvolution.

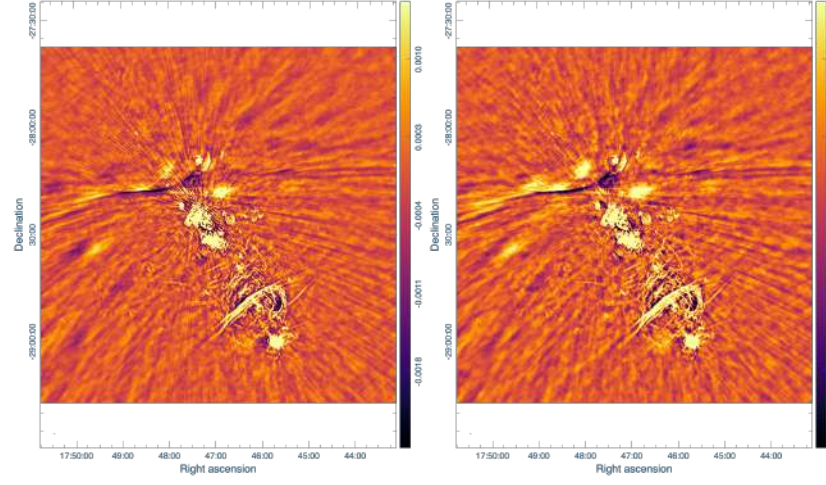


Figure 23: Pointing GC07. The image on the left is a shallow deconvolved image. The image on the right is the one obtained after 3 rounds of self calibration, followed by 2 rounds of deconvolution.

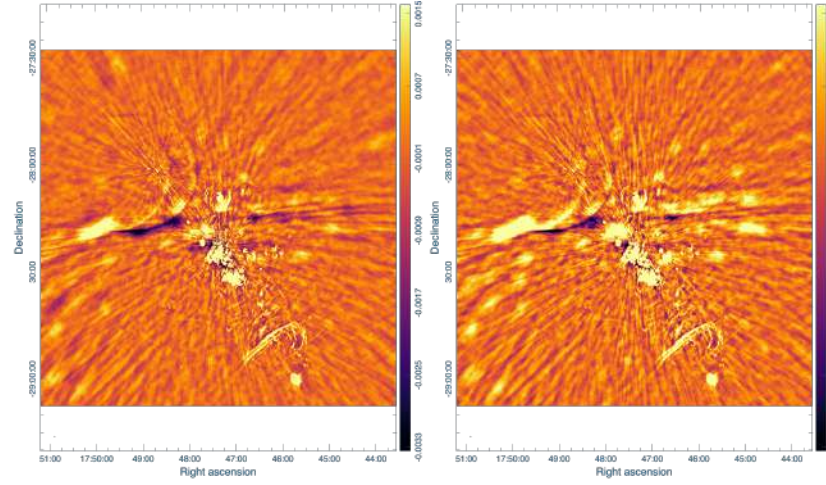


Figure 24: Pointing GC08. The image on the left is a shallow deconvolved image. The image on the right is the one obtained after 3 rounds of self calibration, followed by 2 rounds of deconvolution.



### 3.8 Mosaic: Full extent of Galactic Center at S1

Fig. 25 shows the full extent of the Galactic Center at S1 band of MeerKAT. In the dynamical center of the GC, in Sgr A, the Event Horizon Telescope (EHT) observations show the residing of a supermassive black hole (SMBH) [3] with a mass of about  $4.6 \times 10^6 M_{\odot}$  known as Sgr A\*. There are also HII regions in the GC which are Sgr B1 and B2. Apart from it, there is a bright radio arc which comprises of many non thermal radio filaments (NRFs). They are believed to be the regions arising from synchrotron emitting electrons in the magnetic field structures [4]. There is also a SNR G0.9+0.1, which has the second largest radio pulsar PSR J1747-2809 in the GC [1].

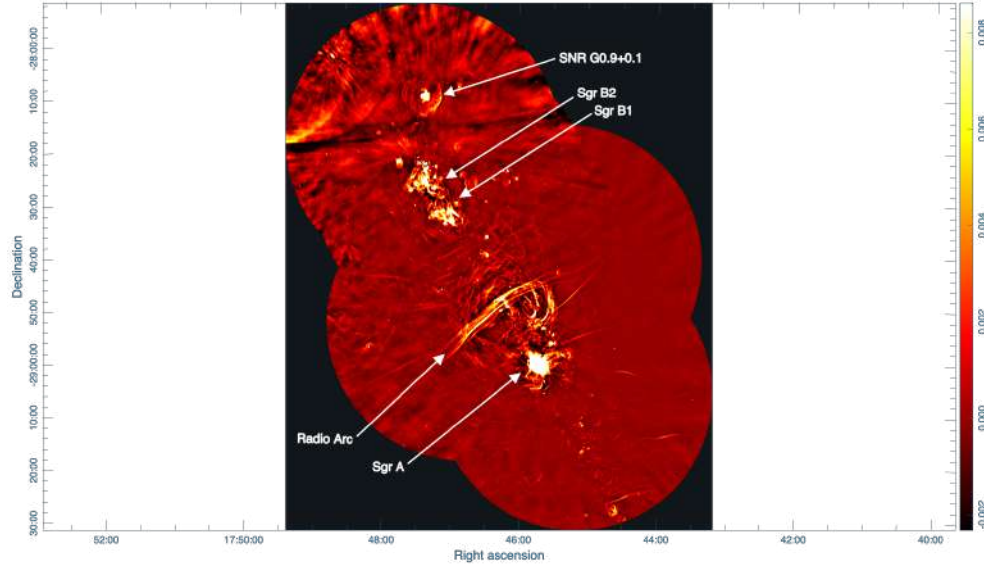


Figure 25: The extent of the Galactic Center pointings GC01-08 at S1 Band of MeerKAT. The images used are primary beam corrected with variance weighting applied to the mosaic. The pointings GC01-GC04 are self calibrated with 3 rounds followed by 5 rounds of deconvolution. The pointings GC05-08 are only self calibrated once in this mosaic and further rounds of self calibration followed by deconvolution needs to be applied on them.

## 4 Summary

To summarize our work, we started with the manual calibration of the target fields GC01-GC04 of the Galactic Center (GC) using the S1 band data of the MeerKAT telescope from the science demonstration project. We examined the data and chose a reference antenna m013 as it had a continuous observation with time as well as is in the compact core of the MeerKAT array. We did first generation calibration (1GC) and used the model spectrum of our primary calibrator J1939-6342 from [11]. Then, we did delay, bandpass and gain calibration. We compared our 1GC gaintable solutions from manual calibration to those from OXKAT and confirmed that the calibration went well. We applied the calibration solutions to all the calibrators and linearly interpolated them to the target fields. The secondary calibrator chosen was J1733-1304, which was assumed to mimic the environment of our target fields. After a shallow deconvolution of the splitted target fields using *wsclean*, we did 3 rounds of self calibration followed by 5 rounds of deconvolution. We primary beam corrected our images and added them in a mosaic using weighted variance to correctly image the primary beam response and to have a constant noise floor.

After that, we used MMGPS pipeline which is the in house pipeline of Max Planck Institute for Radio Astronomy to do 1GC on the target fields GC05-08. We compared the solutions of the MMGPS with those of the OXKAT and confirmed that both the pipelines work well for 1GC calibration. We then did a shallow deconvolution run using *wsclean* which was followed by 3 rounds of self calibration to correct for additional phase errors and 3 rounds of deconvolution for GC05 and GC06 and 2 rounds of deconvolution for GC07 and GC08, to improve the image fidelity, with 30,000 iterations in each run. We primary beam corrected our images and added them in a mosaic using weighted variance to correctly image the primary beam response and to have a constant noise floor.

In the end, we added all the primary beam corrected images for all the target fields together in a mosaic using weighted variance to show full extent of the Galactic

Center at S1 band using the MeerKAT telescope.

We also made the following scripts to ease radio interferometric calibration and imaging. By using these scripts, one can easily plot gain tables, uv coverage of the measurement set and create mosaics.

1. **montage.sh**: To create mosaics.
2. **ragavi.sh**: To generate gainplots after first generation calibration.
3. **shadems.sh**: To plot the uv coverage of the measurement set.

They are available on the GitHub link [here](#), with the instructions to use.

## 5 Future Prospects

The project can be extended further by repeating the procedure described in this report for observations at a different frequency band such as S4. Then one can take all the sub-band images and bring them to the same resolution. The images should be primary beam corrected individually corresponding to their frequency and then one can make spectral index maps from them which will act as a tool to determine the compact objects in the GC. This also leads to multi wavelength study of these determined compact objects before coming to a final conclusion.

## References

- [1] F. Camilo, S. M. Ransom, B. M. Gaensler, and D. R. Lorimer. Discovery of the Energetic Pulsar J1747-2809 in the Supernova Remnant G0.9+0.1. , 700(1):L34–L38, July 2009.

- 
- [2] James J. Cordon and Scott M. Ransom. *Essential Radio Astronomy*. NRAO, 2015.
- [3] Event Horizon Telescope Collaboration and Kazunori Akiyama. First Sagittarius A\* Event Horizon Telescope Results. I. The Shadow of the Supermassive Black Hole in the Center of the Milky Way. , 930(2):L12, May 2022.
- [4] I. Heywood, F. Camilo, W. D. Cotton, F. Yusef-Zadeh, T. D. Abbott, R. M. Adam, M. A. Aldera, E. F. Bauermeister, R. S. Booth, A. G. Botha, D. H. Botha, L. R. S. Brederode, Z. B. Brits, S. J. Buchner, J. P. Burger, J. M. Chalmers, T. Cheetham, D. de Villiers, M. A. Dikgale-Mahlakoana, L. J. du Toit, S. W. P. Esterhuyse, B. L. Fanaroff, A. R. Foley, D. J. Fourie, R. R. G. Gamatham, S. Goedhart, S. Gounden, M. J. Hlakola, C. J. Hoek, A. Hokwana, D. M. Horn, J. M. G. Horrell, B. Hugo, A. R. Isaacson, J. L. Jonas, J. D. B. L. Jordaan, A. F. Joubert, G. I. G. Józsa, R. P. M. Julie, F. B. Kapp, J. S. Kenyon, P. P. A. Kotzé, H. Kriel, T. W. Kusel, R. Lehmensiek, D. Liebenberg, A. Loots, R. T. Lord, B. M. Lunskey, P. S. Macfarlane, L. G. Magnus, C. M. Magozore, O. Mahgoub, J. P. L. Main, J. A. Malan, R. D. Malgas, J. R. Manley, M. D. J. Maree, B. Merry, R. Millenaar, N. Mnyandu, I. P. T. Moeng, T. E. Monama, M. C. Mphego, W. S. New, B. Ngcebetsha, N. Oozeer, A. J. Otto, S. S. Passmoor, A. A. Patel, A. Peens-Hough, S. J. Perkins, S. M. Ratcliffe, R. Renil, A. Rust, S. Salie, L. C. Schwardt, M. Serylak, R. Siebrits, S. K. Sirothia, O. M. Smirnov, L. Sofeya, P. S. Swart, C. Tasse, D. T. Taylor, I. P. Theron, K. Thorat, A. J. Tiplady, S. Tshongweni, T. J. van Balla, A. van der Byl, C. van der Merwe, C. L. van Dyk, R. Van Rooyen, V. Van Tonder, R. Van Wyk, B. H. Wallace, M. G. Welz, and L. P. Williams. Inflation of 430-parsec bipolar radio bubbles in the Galactic Centre by an energetic event. , 573(7773):235–237, September 2019.
- [5] I. Heywood, I. Rammala, F. Camilo, W. D. Cotton, F. Yusef-Zadeh, T. D. Abbott, R. M. Adam, G. Adams, M. A. Aldera, K. M. B. Asad, E. F. Bauermeister, T. G. H. Bennett, H. L. Bester, W. A. Bode, D. H. Botha, A. G. Botha,

L. R. S. Brederode, S. Buchner, J. P. Burger, T. Cheetham, D. I. L. de Villiers, M. A. Dikgale-Mahlakoana, L. J. du Toit, S. W. P. Esterhuyse, B. L. Fanaroff, S. February, D. J. Fourie, B. S. Frank, R. R. G. Gamatham, M. Geyer, S. Goedhart, M. Gouws, S. C. Gumede, M. J. Hlakola, A. Hokwana, S. W. Hoosen, J. M. G. Horrell, B. Hugo, A. I. Isaacson, G. I. G. Józsa, J. L. Jonas, A. F. Joubert, R. P. M. Julie, F. B. Kapp, J. S. Kenyon, P. P. A. Kotzé, N. Kriek, H. Kriel, V. K. Krishnan, R. Lehmensiek, D. Liebenberg, R. T. Lord, B. M. Lunsy, K. Madisa, L. G. Magnus, O. Mahgoub, A. Makhaba, S. Makhathini, J. A. Malan, J. R. Manley, S. J. Marais, A. Martens, T. Mauch, B. C. Merry, R. P. Millenaar, N. Mnyandu, O. J. Mokone, T. E. Monama, M. C. Mphego, W. S. New, B. Ngcebetsha, K. J. Ngoasheng, M. T. Ockards, N. Oozeer, A. J. Otto, S. S. Passmoor, A. A. Patel, A. Peens-Hough, S. J. Perkins, A. J. T. Ramaila, N. M. R. Ramanujam, Z. R. Ramudzuli, S. M. Ratcliffe, A. Robyn-tjies, S. Salie, N. Sambu, C. T. G. Schollar, L. C. Schwardt, R. L. Schwartz, M. Serylak, R. Siebrits, S. K. Sirothia, M. Slabber, O. M. Smirnov, L. Sofeya, B. Taljaard, C. Tasse, A. J. Tiplady, O. Toruvanda, S. N. Twum, T. J. van Balla, A. van der Byl, C. van der Merwe, V. Van Tonder, R. Van Wyk, A. J. Venter, M. Venter, B. H. Wallace, M. G. Welz, L. P. Williams, and B. Xaia. The 1.28 GHz MeerKAT Galactic Center Mosaic. , 925(2):165, February 2022.

- [6] D. R. Lorimer and M. Kramer. *Handbook of Pulsar Astronomy*, volume 4. 2004.
- [7] NRAO. VLA continuum tutorial 3c391-casa6.4.1. [https://casaguides.nrao.edu/index.php?title=VLA\\_Continuum\\_Tutorial\\_3C391-CASA6.4.1#Bandpass\\_Calibration](https://casaguides.nrao.edu/index.php?title=VLA_Continuum_Tutorial_3C391-CASA6.4.1#Bandpass_Calibration), February 2023.
- [8] A. R. Offringa, B. McKinley, N. Hurley-Walker, F. H. Briggs, R. B. Wayth, D. L. Kaplan, M. E. Bell, L. Feng, A. R. Neben, J. D. Hughes, J. Rhee, T. Murphy, N. D. R. Bhat, G. Bernardi, J. D. Bowman, R. J. Cappallo, B. E. Corey, A. A. Deshpande, D. Emrich, A. Ewall-Wice, B. M. Gaensler, R. Goeke, L. J. Greenhill, B. J. Hazelton, L. Hindson, M. Johnston-Hollitt, D. C. Jacobs, J. C. Kasper, E. Kratzenberg, E. Lenc, C. J. Lonsdale, M. J. Lynch, S. R. McWhirter, D. A.

- Mitchell, M. F. Morales, E. Morgan, N. Kudryavtseva, D. Oberoi, S. M. Ord, B. Pindor, P. Procopio, T. Prabu, J. Riding, D. A. Roshi, N. Udaya Shankar, K. S. Srivani, R. Subrahmanyam, S. J. Tingay, M. Waterson, R. L. Webster, A. R. Whitney, A. Williams, and C. L. Williams. WSCLEAN: an implementation of a fast, generic wide-field imager for radio astronomy. , 444(1):606–619, October 2014.
- [9] Isabella Dineo Rammala. Discovery and classification of compact radio sources in the meerkat galactic centre data, November 2022.
- [10] Shilpa Ranchod. A deep meerkat search for neutral hydrogen in, and lensed by, dense environments, February 2021.
- [11] J. Reynolds. A revised flux scale for the at compact array, July 1994.
- [12] SARAo. S-band capability and status. <https://skaafrica.atlassian.net/wiki/spaces/ESDKB/pages/1588854789/S-band+capability+and+status>, April 2023.
- [13] O. M. Smirnov. Revisiting the radio interferometer measurement equation. I. A full-sky Jones formalism. , 527:A106, March 2011.